AIAA JOURNAL
Vol. 39, No. 12, December 2001

Fuel–Air Mixing Enhancement by Synthetic Microjets

H. Wang* and S. Menon†
Georgia Institute of Technology, Atlanta, Georgia 30332-0150

Next-generation combustors must maintain combustion efficiency while considerably reducing emissions, such as CO, NO$_x$, and unburned hydrocarbons. A viable methodology is to enhance the fuel–air mixing process so that the initial dense spray regime is minimized and the subsequent mixing between the vaporized fuel and air is maximized. Current investigations of mixing methods using microelectromechanical systems (MEMS)-based microjet injectors have demonstrated a possible active control technique for rapidly increasing the mixing process. However, detailed understanding of the coupling between the MEMS device and the fuel injector is not yet available. Here, a Lattice Boltzmann Equation method (which is computationally much more efficient than the conventional finite-volume approach) is employed to simulate the flow both inside and outside a synthetic jet actuator. The effects of varying the forcing amplitude and frequencies and different configurations of the synthetic actuators are examined in order to evaluate sensitivity of the actuation to design parameters. Subsequently, the synthetic jets are integrated within a typical fuel injector, and the efficiency of the microactuation on fuel–air mixing is addressed. It is shown that synthetic microjets embedded inside the fuel injector can provide a mechanism for significantly enhancing fuel–air mixing. Implications for practical applications are also discussed.

Introduction

NEXT-GENERATION aircraft gas turbine engines are required to satisfy severe emission constraints mandated by federal and international requirements. Maintaining combustion efficiency and flame stability while simultaneously reducing NO$_x$ (and CO and unburned hydrocarbons during takeoff/landing) emissions is not feasible without innovative changes in the combustor design.

Current attempts are focussed on modifying/controling the fuel–air mixing by changing the pattern of the fuel injected into the combustor. Designs such as multiple injection using microlaminate screens and advanced swirler cups are currently under study. These concepts are methods that can quickly break up the initial dense spray regime to develop a relatively well-characterized dilute spray pattern so that both the fuel–air mixing and the subsequent combustion process can be controlled as required. The dense spray regime, which occurs as the liquid fuel exits from the nozzle (and, therefore, plays a determining role in the subsequent spray pattern), is a major area of uncertainty because the process of liquid breakup, the formation of ligaments followed by ligament stretching and turbulence-induced distortion, and, finally, breakup are not understood very well. Thus, it is clear that an approach which will minimize, if not eliminate, the dense spray regime could go a long way toward developing a controlled spray pattern and, hence, allow efficient fuel–air mixing.

An underlying feature of the just-noted design concepts is the passive approach to mixing enhancement. This has been necessary because the fuel injectors have to operate in a hostile (hot) environment and must deliver the requisite fuel pattern over a wide operating regime. Active control of fuel injection has only recently been explored, and recent results suggest that robust active control methods could extend the operating margin of the fuel-injection system. Such an approach has the potential for providing a new means for controlling the combustion process even under conditions that are not allowed to occur in current designs. For example, flame stability in the lean limit, control during high-pressure combustion, and efficient combustion using new (supercritical) fuels are all potential operational scenarios that may be achieved using active control.

As an example of recent innovation, experiments have demonstrated the ability of microelectromechanical systems (MEMS) such as microinjectors and synthetic jet actuators[1–4] to control and modify the dynamics of primary jet flow. Experiments have shown that the primary jet spreading rate can be significantly enhanced by using these microinjectors along the circumference of the jet nozzle. An obvious practical application is enhancement of fuel–air mixing. These microinjectors may function as expected in real combustors if they are inside the primary fuel injector nozzle and, therefore, relatively protected from the hot environment. So far, the effects of the MEMS devices have been ascertained only indirectly by observing the primary jet flow because detailed quantitative measurements in the vicinity of the microinjectors are difficult, if not impossible. Furthermore, all studies so far have been limited to nonreacting flows and to relatively large devices. For example, in recent studies synthetic jets with exit diameter of 8 mm were used to enhance mixing in a primary air jet of around 25 mm. However, real fuel injectors have typical diameters of 1–3 mm, which implies that the synthetic jet diameter needs to be around 0.1 mm or smaller. Under these conditions detailed measurements in the near field are going to be very difficult.

To demonstrate the ability of MEMS devices to control fuel injectors in a practical combustor optimization of these devices (including design, placement, and forcing conditions) is required. Although this could be attempted experimentally, a numerical predictive capability, if available, would go a long way toward providing the additional data on the near-field flow dynamics for optimal design. Recently, some numerical studies of the flowfield in the vicinity of a synthetic jet have been reported.[5–7] However, these studies were limited to nonreacting, single-phase flows and simulated the synthetic jet in isolation. Thus, the coupling of the synthetic jet with the primary fuel jet has not yet been investigated.

The just-noted numerical studies[5–7] were carried out using conventional Navier–Stokes codes. Although this approach is acceptable for conditions of interest here, the computational cost of resolving the flow both inside and outside the synthetic jet and in the combustor using a single finite difference formulation can be quite severe. For example, a typical gas turbine combustor (e.g., General Electric LM 6000) is around 15 cm long, whereas a typical fuel injector diameter is around 3 mm. A synthetic jet inside the fuel injector has to be even smaller, with an orifice diameter of 0.1–0.2 mm. For proper resolution of the interaction, both the cavity and the jet orifice need to be well resolved. Furthermore, to resolve the combustion process in the combustor the combustor also needs to be resolved adequately. In a typical finite-volume large-eddy simulation (LES) technique resolving all of these disparate scales will

---

Received 26 July 2000; revision received 15 June 2001; accepted for publication 18 June 2001.

*Graduate Assistant, School of Aerospace Engineering.

†Professor, School of Aerospace Engineering. Associate Fellow AIAA.

require prohibitive resolution (and also a very small time step, which will further increase the overall cost).

An alternate methodology that is computationally much more efficient is the Lattice Boltzmann Equation (LBE) method.[8–12] This method has been demonstrated in various types of flows including two-phase and reacting flows.[11,12] Results have demonstrated that the LBE method 1) can be used to study flows in complex three-dimensional configurations (a requirement essential to simulate microinjectors of current interest),[9] 2) reproduces the Navier–Stokes equations in the continuum limit, 3) is computationally very efficient and inherently parallel, and 4) is applicable to low-Reynolds-number and low-Mach-number flows (typical inside the synthetic injectors). Another advantage of the LBE method is that it has the potential for application even in the transition regime (near continuum, $0.1 < Kn < 1$, where Kn is the Knudsen number) by proper modifications to the collision integral in the Boltzmann equation.

This paper discusses the application of LBE method to simulate the flow both inside and outside a synthetic jet. Further, this model is used to simulate a fully coupled scenario in which the microsynthetic jets are used to excite (i.e., force) a fuel jet. The effect of the microjet on scalar mixing efficiency is also addressed in this study. The eventual goal of this research is to employ the LBE method to simulate the flow inside the synthetic microjet and the fuel injector and to combine this model with a subgrid combustion model[13,14] in a finite volume LES solver. Coupled LBE-LES simulations are currently underway but will be the focus of a future presentation.

This paper is organized as follows. The LBE method is described in the next section, and then the simulation methodology is summarized in the following section. This is followed by a results and discussion section, and then, conclusions are summarized in the final section.

Lattice Boltzmann Method

The Boltzmann equation is the fundamental equation that governs all fluid motion from free molecular flow to continuum flow. This equation is derived using kinetic theory and is an equation for the probability density function for the molecular motion in phase space. The phase space is a seven-dimension space: the physical space $\boldsymbol{x}$, the velocity space $\boldsymbol{v}$, and time t. The equation governing the evolution of the pdf of the molecular distribution $f(\boldsymbol{x}, \boldsymbol{v}, t)$ when integrated over the velocity space (using Chapman–Enskog expansion) recovers the well-known continuum Navier–Stokes equations of motion.

In the LBE method the kinetic equation for the Boltzmann distribution function is solved and can be viewed as a type of finite difference solution of the Boltzmann equation. There are some significant advantages of this approach. The LBE method recovers the Navier–Stokes equation in the low-frequency and long-wavelength limit and is Galilean invariant (see cited references). In application, this method is purely local, inherently parallel, and very fast. An important feature is that (unlike conventional finite-difference methods) LBE method has the same speed and efficiency in both simple and complex geometries.[11,12,15] Properly optimized parallel codes have been developed in the past and have demonstrated near teraflop capability.[12] Furthermore, these methods can be used for both compressible and incompressible three-dimensional flows.[12,16,17]

Nine-Velocity LBE model

The LBE method solves the Boltzmann equation in the phase space (physical space, velocity space, and time). A recent study[18] showed that the LBE method can also be regarded as a discrete form of the continuous Boltzmann equation, providing that the discretization has a certain order of accuracy.

The key step in the LBE method's implementation is the manner in which the velocity space discretization is carried out. The nine-velocity LBE model[8,19] (see Appendices) has been shown to be sufficient to recover the Navier–Stokes equations in two-dimensional flows. In three-dimensional flows (to be studied in the future), 18-velocity directions are needed to recover the full three-dimensional Navier–Stokes equations.[12]

The nine-velocity LBE model simulates fluid flow by tracking the single-particle distribution function at the following nine discrete (nondimensional) velocities:

$$\boldsymbol{e}_\alpha = \begin{cases} 0, & \alpha = 0 \\ (\cos[\alpha^*], \sin[\alpha^*])c, & \alpha = 1-4 \\ \sqrt{2}(\cos[\alpha''], \sin[\alpha''])c, & \alpha = 5-8 \end{cases} \tag{1}$$

where $\alpha^* = (\alpha - 1)\pi/2$, $\alpha'' = (\alpha - 5)\pi/2 + \pi/4$, and c is a characteristic speed, which is related to the sound speed by $c = \sqrt{3}c_s$ (Refs. 12 and 19). Rest particles of type 0 with $e_0 = 0$ are also allowed in this formulation.

The evolution of the distribution functions f_α for $\alpha = 0, 1, \ldots, 8$ is governed by

$$f_\alpha(\boldsymbol{x} + \boldsymbol{e}_\alpha\delta, t + \delta) - f_\alpha(\boldsymbol{x}, t) = (1/\tau)\left[f_\alpha^{eq}(\boldsymbol{x}, t) - f_\alpha(\boldsymbol{x}, t)\right] \tag{2}$$

where τ is the dimensionless relaxation time, $\boldsymbol{e}_\alpha$ is the particle speed in the α direction, and the characteristic speed is $c = \boldsymbol{e}_\alpha\delta/\delta = |\boldsymbol{e}_\alpha|$.[12,18] The equilibrium distribution function f_α^{eq} is[12,18,19]

$$f_\alpha^{eq} = w_\alpha \rho\left[1 + \frac{3(\boldsymbol{e}_\alpha \cdot \boldsymbol{u})}{c^2} + \frac{9}{2}\frac{(\boldsymbol{e}_\alpha \cdot \boldsymbol{u})^2}{c^4} - \frac{3}{2}\frac{\boldsymbol{u}^2}{c^2}\right] \tag{3}$$

where

$$w_\alpha = \begin{cases} \frac{4}{9}, & \alpha = 0 \\ \frac{1}{9}, & \alpha = 1, 2, 3, 4 \\ \frac{1}{36}, & \alpha = 5, 6, 7, 8 \end{cases}$$

Solution of Eq. (2) gives f_α, which can then be used to obtain the macroscopic variables. For example, the density ρ and the velocity field $\boldsymbol{u}$ are calculated by

$$\rho = \sum_\alpha f_\alpha \tag{4}$$

$$\rho\boldsymbol{u} = \sum_\alpha \boldsymbol{e}_\alpha f_\alpha, \qquad \alpha = 0, 1, \ldots, 8 \tag{5}$$

It has been shown that if Chapman–Enskog procedure is applied to Eq. (2) the macroscopic equations of the model (i.e., the Navier–Stokes equations) are recovered in the following form (details have been reported elsewhere[12,16,18–21] and, therefore, omitted here for brevity):

$$\frac{\partial\rho}{\partial t} + \frac{\partial\rho u_\alpha}{\partial x_\alpha} = 0 \tag{6}$$

$$\frac{\partial(\rho u_\alpha)}{\partial t} + \frac{\partial}{\partial x_\beta}(\rho u_\alpha u_\beta) = \frac{\partial p}{\partial x_\alpha} + \frac{\partial}{\partial x_\beta}(2\nu\rho S_{\alpha\beta}) \tag{7}$$

Here, repeated indices indicate summation $S_{\alpha\beta} = \frac{1}{2}(\partial u_\beta/\partial x_\alpha + \partial u_\alpha/\partial x_\beta)$ is the strain-rate tensor, the pressure is $p = c_s^2\rho$, and $\nu = [(2\tau - 1)/6]$ is the kinematic viscosity. The preceding equations reduce to the incompressible Navier–Stokes equation when $\rho = \text{const}$. Model equations for zero-Mach-number flows (i.e., incompressible flows with reactions) and for compressible flows have also been derived and used in the past.[12,22]

Simulation Methodology

The numerical simulation using the LBE method involves three steps: collision, streaming, and interpolation. Given an initial particle distribution function f_α at each of the lattice location $\boldsymbol{x}$, all macroscopic flow properties such as the velocities u, v, and pressure p are known. Also, the equilibrium distribution function f_α^{eq} can be constructed at every lattice point. Then, in the first step collisions take place according to the right-hand side of Eq. (2). From this step the postcollision value of f_α can be determined. After collisions, advection (also called streaming) takes place at every lattice point, and the values of $f_\alpha(\boldsymbol{x} + \boldsymbol{e}_\alpha\delta, t + \delta)$ are obtained. In the final step the values of $f_\alpha(\boldsymbol{x}, t + \delta)$ on the mesh grid $\boldsymbol{x}$ are computed from the values of $f_\alpha(\boldsymbol{x} + \boldsymbol{e}_\alpha\delta, t + \delta)$ on the lattice points $\boldsymbol{x} + \boldsymbol{e}_\alpha\delta$ by interpolation. This last step is only needed if a nonuniform lattice is used (as done here). Then, the collision and the advection steps are repeated.

The model used here has been shown to be second-order accurate in space and time.[23] Accuracy of the scheme is achieved by proper interpolation method when applied on nonuniform grids as well as by using accurate boundary conditions.[10,15,23,24] The implementation of the boundary conditions is especially critical for obtaining correct solution and is described in Appendix A. (These conditions follow earlier development of similar models.[25])

Scalar LBE Model

In this study scalar mixing is investigated using the LBE method. To simulate scalar (temperature or species) evolution, a two-component LBE system was demonstrated earlier.[10,26] (Extension to two-phase and reacting flows has also been demonstrated earlier.[12]) The distribution functions for two components ($i = 1, 2$) evolve according to Eq. (2) and can be expressed as

$$f_\alpha^{(i)}(\boldsymbol{x}+\boldsymbol{e}_\alpha\delta, t+\delta) - f_\alpha^{(i)}(\boldsymbol{x}, t) = \left[1/\tau^{(i)}\right]\left[f_\alpha^{(i,eq)}(\boldsymbol{x}, t) - f_\alpha^{(i)}(\boldsymbol{x}, t)\right] \tag{8}$$

In this model component 1 represents the motion of the fluid, and component 2 simulates a passive scalar field. The equilibrium distributions for both components are still defined by Eq. (3). Because component 2 is passively advected and diffuses into the flow of component 1 without contributing to the total momentum of the mixture (in the present study), the velocity $\boldsymbol{u}$ in the equilibrium distribution of component 2 is replaced by the fluid velocity calculated from the distribution function of component 1.

The density and the fluid velocity of component 1 still satisfy the Navier–Stokes conservation equations, and the density of component 2 satisfies the conventional diffusion equation of a passive scalar. The diffusivity of component 2, D can be tuned independent of the viscosity ν by changing the dimensionless relaxation time τ of the component 2. In the present study we assume that the Schmidt number $Sc = \nu/D$ is unity, which is reasonable for gas phase scalar mixing.

Extension to Nonuniform Grid

The original LBE models were restricted to a uniform lattice in the physical space. Thus, a particle (or an equilibrium distribution) had to move to another lattice site at each time step. However, because the particle distribution in LBE models is a continuous function in both space and time the value of a function at one location in space can be interpolated from the values of the function at the neighboring locations.

Based on this observation, an interpolation supplemented LBE (ISLBE) model was demonstrated for simulations in nonuniform grids.[23,27] Numerical simulations of flow in a sudden expansion[27] and flow around a circular cylinder[28] using the ISLBE model agreed quite well with benchmark data. Theoretical analysis also showed that the ISLBE is at least second-order accurate when a quadratic interpolation scheme is used. The same approach is used in the present study. (Details are avoided here, for brevity.)

Boundary Conditions

The boundary conditions are especially critical in order to use the LBE approach. Application of the boundary conditions for no-slip, catalytic walls as well as inflow and outflow conditions, especially for the two-fluid problem, require special considerations. These boundary conditions involve subtle implementation issues[25,29,30] that are described in some detail in Appendices A and B.

Results and Discussion

The results are summarized in this section. First, the flowfield both inside and outside a synthetic jet is simulated, and the effect of various design parameters is investigated to determine the sensitivity of the device. Then, a typical fuel injector with these synthetic jets embedded inside the injectors is simulated to evaluate scalar mixing efficiency of the synthetic jets.

Synthetic Jet Simulations

A single synthetic jet is first simulated to investigate the efficiency of actuation as a function of design parameters. Figures 1a and 1b show, respectively, a typical synthetic jet and a grid distribution. The flow inside the cavity and downstream of the orifice exit plane are simulated. In actual experiments the synthetic jet is triggered by vibrating the bottom wall of the cavity (which is made of a piezoelectric material). It is difficult (although not impossible) to mimic this feature in a numerical model. The primary result of the surface actuation is that the fluid adjacent to the oscillating surface is set into motion. Therefore, in the present study this resulting phenomenon is mimicked by incorporating a blowing/suction boundary condition (with no net mass loss) along the bottom wall of the cavity. This approach, therefore, ignores the physical movement of the bottom but provides an appropriate boundary condition to modify the fluid motion inside the cavity (as in the real device). No explicit control of the flow exiting from the cavity orifice is needed. Earlier studies[5] imposed the perturbation to the streamwise velocity component at the orifice exit itself. This approach imposes a restriction on the flow exiting (and entering) the cavity that is not likely to be realistic. More recent studies[6] have addressed this deficiency and simulated the flowfield inside the cavity as well.

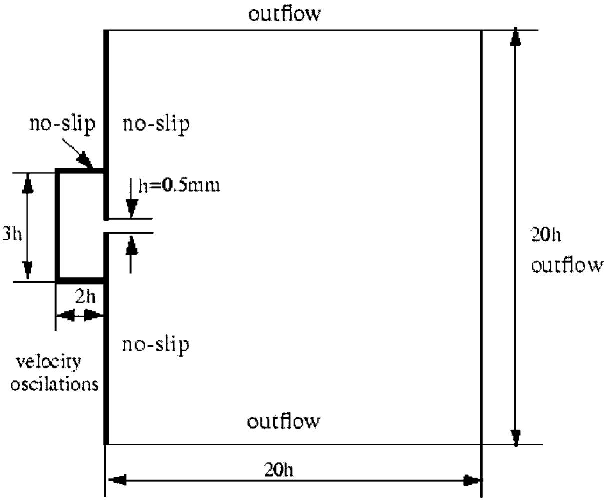

Fig. 1a Computational domain.

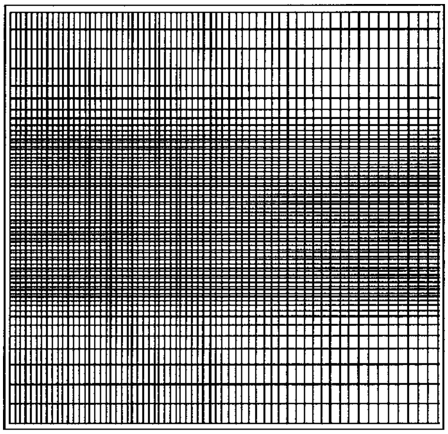

Fig. 1b Typical grid resolution.

The streamwise velocity perturbation (with zero mean) at the bottom wall of the cavity is of the form $u(t) = U_0 \sin \omega t$, where ω is the prescribed frequency and U_0 is the forcing amplitude. The effect of varying the forcing frequency, the forcing amplitude, the cavity depth, and the orifice size is investigated. However, for brevity, we discuss only representative cases. The various cases are summarized in Table 1. The baseline values are $U_0 = 20$ m/s, $d_0 = 1$ mm, $h_0 = 0.5$ mm, and $f_0 = 4$ KHz. These value are within the range for practical implementation within real fuel injectors and also within a parameter space where some experimental data are available for comparison. Based on the forcing frequency and the orifice diameter, the Strouhal number of the forcing is 0.1, which is within the range of the jet preferred mode.[31] We use case 11 (which is similar to an earlier experiment) to carry out validation of the present synthetic jet model. Other cases are used to characterize the behavior of the

Table 1 Computational cases for synthetic jets

Type	Forcing amplitude	Forcing frequency	Orifice size	Cavity depth	$Sr = f_0h_0/U_0$	$Re = U_0H_0/\nu$
Case 1	U_0	f_0	h_0	$2h_0$	0.1333	635
Case 2	U_0	$0.5f_0$	h_0	$2h_0$	0.0667	635
Case 3	U_0	$2f_0$	h_0	$2h_0$	0.2667	635
Case 4	$0.5U_0$	f_0	h_0	$2h_0$	0.2667	317
Case 5	$1.5U_0$	f_0	h_0	$2h_0$	0.0889	952.5
Case 6	U_0	f_0	$1.5h_0$	$2h_0$	0.2	952.5
Case 7	U_0	f_0	$2h_0$	$2h_0$	0.2667	1270
Case 8	U_0	f_0	$2h_0$	h_0	0.2667	1270
Case 9	U_0	f_0	h_0	$4h_0$	0.1333	635
Case 10	U_0	f_0	h_0	$10h_0$	0.1333	635
Case 11	$1.25U_0$	$0.5f_0$	h_0	$2h_0$	0.05333	793
Case 12	$0.5U_0$	$2f_0$	h_0	$2h_0$	0.5332	317
Case 13	U_0	f_0	$0.5h_0$	$2h_0$	0.6667	317
Case 14	U_0	f_0	$0.1h_0$	$2h_0$	0.013	63
Case 15	U_0	$4f_0$	h_0	$2h_0$	0.6667	635

synthetic jet under various conditions. For parametric comparison case 1 is used as the baseline case.

To analyze the results, data were collected after two flow-through times for a period of around six to eight flow-through times. (Here, a flow-through time is defined as the time it takes for a shed vortex to leave the computational domain.) These data were then time averaged to obtain the stationary state results.

Very high grid resolution is employed for all of the present simulations. Figure 1b shows the typical grid used for the simulations. The grid is clustered in regions of high shear such as the jet orifice. (Approximately 20 grid points are used to resolve the orifice.) Furthermore, to ensure that the flowfield in the cavity is well resolved, a large number of grid points (approximately 60×40) is used in that region. Grid is also clustered near all of the wall regions. To resolve the entire domain, grid needs to be stretched from these regions of high resolution. However, to maintain second-order accuracy the grid stretching is sufficiently small: a stretching factor of 1.005 in the streamwise direction and 1.045 in the cross-stream direction is employed.

Various grid resolution simulations were carried out to determine grid independence. We compared simulations using grids of 260×285, 321×325, and 375×525. The resolution was increased in the cross-stream direction primarily to ensure that the regions of high shear are sufficiently resolved. As shown elsewhere,[32] there are no noticeable differences between the results obtained using these grids. Therefore, all results reported here employed the intermediate resolution of 321×325.

Note that although this resolution appears quite large the unique advantage of the LBE method is that even with such a high resolution, a typical simulation (i.e., around 10 flow-through times) can be completed overnight on a single processor SGI Origin. This is contrasted to the computational time of several days when using a conventional finite volume scheme. The primary reason is that the LBE method solves a single scalar equation, whereas conventional methods solve the full Navier–Stokes equations. Therefore, in spite of the high grid resolution employed here the LBE simulations are considered cost effective. Parallel implementation of the LBE model can further reduce the computational cost.

Finally, because very high resolution is employed these simulations are deemed direct numerical simulations, albeit in two dimensionality. However, because the flowfield is generated using jet preferred mode forcing the shed vortices in the near field are likely to be primarily axisymmteric (i.e., with significant azimuthal coherence).[31] Thus, many features observed here are likely to be similar to features in real systems. Of course, in the far field, where ambient turbulence and three-dimensional vortex stretching effects are likely to dominate, the present two-dimensional simulations are expected deviate from the observations. Simulation of this flowfield using a full three-dimensional LBE model is currently being initiated in order to confirm and verify the results reported here.

Structure of the Flowfield

As observed in the experiments, when forcing is applied at the bottom of the cavity a periodic fluid motion occurs through the cavity orifice. In the absence of mean flow, the sinusoidal forcing generates no net mass flow but introduces momentum. This is a unique feature of the synthetic jet. During the outflow portion of the forcing cycle as the fluid exits from the orifice because of the shear relative to the surrounding external flow a vortex ring is shed from the orifice lip. This vortex ring propagates downstream at a velocity close to the forcing amplitude U_0. Continuing the forcing results in a periodic shedding of these vortex rings at the forcing frequency, as shown in Fig. 2. This flow feature is in good agreement with experimental observations in the near field. The shed vortices propagate downstream at a relatively constant velocity without significant decay. However, note that the coherence of the shed vortices far downstream is probably an artifact of the present two-dimensional simulation because no ambient turbulence and/or three-dimensional effects are included here. Experimental data in turbulent flows suggest that as the shed vortices propagate away from the orifice they begin to diffuse and break down as a result of three-dimensional turbulence and vortex stretching effects. Although this feature is not captured here, in the near field (were turbulence effects have not yet begun to effect the coherence of the shed vortices) the present results are in good agreement with experimental observations (see further comments in the following).

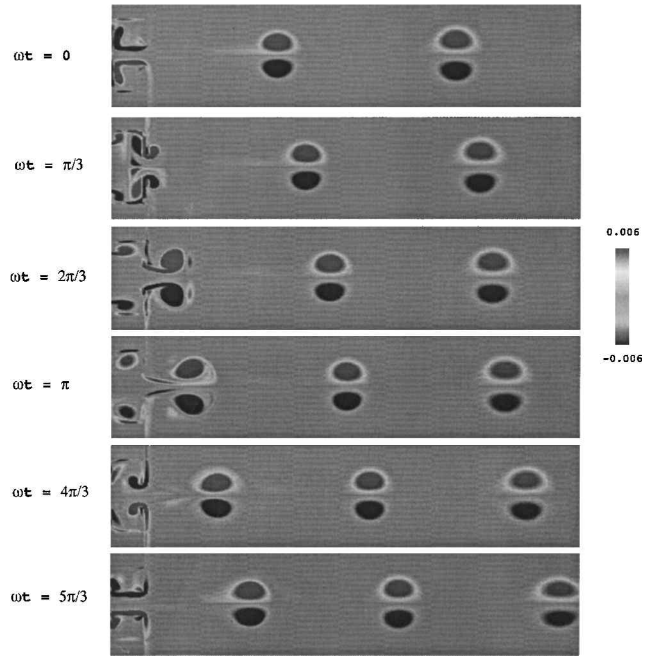

Fig. 2 Vorticity contours outside the synthetic jet for case 1.

Figure 3 shows the instantaneous vorticity contour sequence inside the synthetic jet cavity for case 1. At $\omega t = \pi/3$ outflow is just beginning, and the formation of primary vortices can be seen. At around $\omega t = 4\pi/3$ the shed vortex is moving away from the orifice,

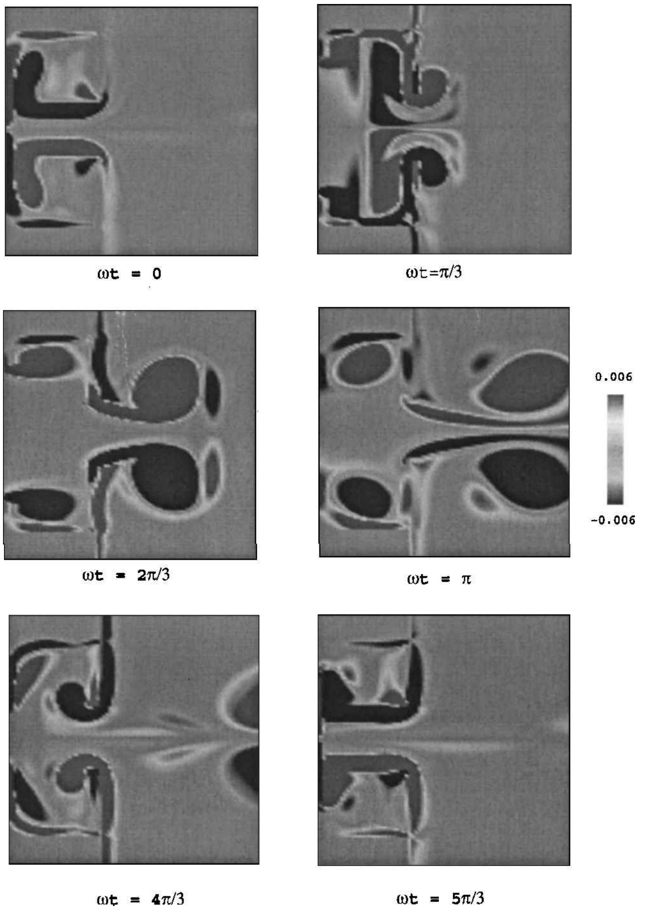

Fig. 3 Vorticity contours inside the synthetic jet cavity for case 1.

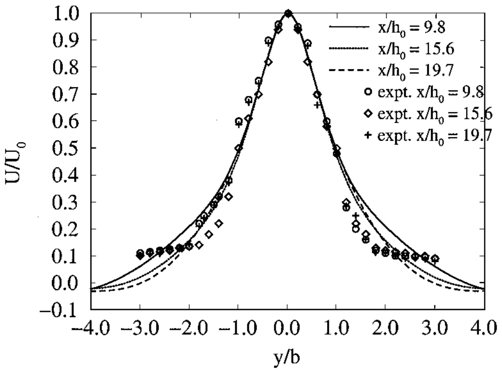

Fig. 4 Comparison of the normalized velocity profiles at various axial locations with experimental data.[3]

and the suction cycle is just beginning. During the suction period, vortex shedding also occurs inside the cavity. This vortex impinges on the bottom wall (as in an impinging jet) and spreads along the bottom wall and up the side wall (as shown at $\omega t = 0$). A portion of this wall boundary layer becomes part of the vortex that is shed from the orifice during the next cycle. Before the suction period begins, the vortex ring shed outside the cavity has already moved out into the external fluid. As a result, the flow sucked into the cavity during the next cycle does not affect the shed vortex, and analysis shows that a majority of the sucked fluid comes from the wall boundary layers on the outside of the cavity. This behavior is an experimentally observed feature of the synthetic jet actuator.

As just noted, case 11 corresponds closely to test conditions in some of the early experiments. Figure 4 compares the predicted (normalized) velocity profiles at various axial locations with experimental data.[3] There is reasonable agreement in the central region of the jet indicating that self-similar evolution has been achieved. There are, however, some discrepancies at the outer edges of the jet shear layer. This region is highly intermittent and turbulent in the experiments and is also where significant three-dimensional effects such as vortex stretching and breakdown occurs. Full three-dimensional LBE (currently under development) simulations may be able to predict better the flow in this region.

Sensitivity to Design Parameters

All cases summarized in Table 1 were studied to investigate the sensitivity of the synthetic jet to the various parameters.[32] However, for brevity, only a few cases are shown and discussed here. Qualitative and quantitative comparison of the various cases with the reference case 1 is discussed next.

When the orifice size is increased (cases 6–8), comparison with case 1 indicates some significant differences. As the orifice size is increased, the vortex shed during the injection period of the forcing cycle becomes smaller. This is probably related to the redistribution of the momentum through the orifice because the same amount of momentum is being spread out over a larger area. On the other hand, decreasing the orifice size to very small also is not very effective because when the size becomes very small the viscous effects in the small orifice dissipates the momentum. Thus, it appears that in order to maintain coherence of the initial vortex ring the orifice size needs to be of a certain size for a given forcing frequency and amplitude.

Changing the cavity depth affects the flow dynamics both outside and inside the cavity. Decreasing the cavity depth (case 8, not shown) does not appreciably affect the coherence and size of the vortices shed from the cavity. However, when the cavity depth is increased (case 9, also not shown, brevity) there is a larger region of internal motion in the cavity, and some of its momentum is used to create a large vortex pair that propagates inside the cavity in a manner quite similar to the propagation seen outside the cavity. However, the shed vortex appears to be relatively weaker when compared to the other cases.

Thus, it can be concluded that changing the jet cavity dimensions can also have appreciable effect on the shed vortices and the net momentum transferred into the external flow. There appears to be an optimal configuration for a given forcing frequency.

Mass and Momentum Flux Analysis

The mass flux through the orifice was computed for all of the cases to determine the effectiveness of the actuation process. Figure 5 shows the temporal variation of the mass flow rate through the orifice of the actuator for various forcing amplitude (cases 1, 4, and 5). The mass flux is normalized by the mass flux based on the maximum forcing velocity. The time-averaged mass flux through the orifice is zero even though there are some cycle-to-cycle variations. Figure 5 also shows that as the forcing amplitude increases the amount of mass moved through the orifice also increases. However, there is not much effect on the net mass flux when the orifice size is changed or when the cavity depth is changed.[32]

Analysis of the momentum flux through the orifice and momentum at a fixed downstream location was also carried out. Figure 6 shows the momentum flux through the orifice and the momentum flux at $x/h = 11.8$ for case 1. Although the net momentum through the orifice is zero, farther downstream (e.g., at $x/h = 11.8$) it is positive during any given cycle. This is the unique feature of the synthetic jet, and the present simulation has captured it quite well.

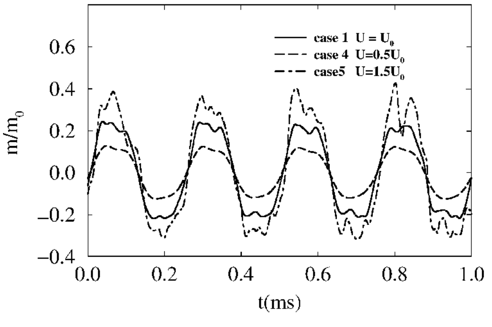

Fig. 5 Mass flux through the orifice for various forcing amplitudes.

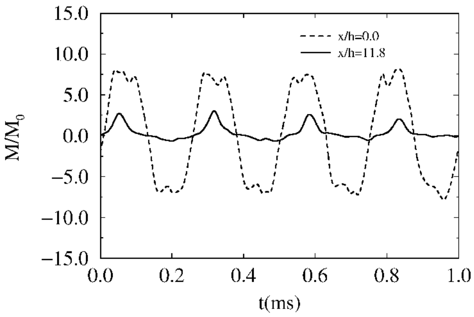

Fig. 6 Momentum flux balance at the orifice and at a distance ($x/h = 11.8$) downstream from the orifice. A net positive momentum is imparted into the fluid by the actuation that is felt far downstream.

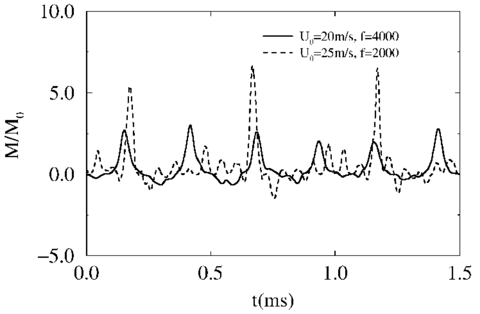

Fig. 7 Effect of forcing frequency on the momentum flux balance at $x/h = 11.8$ (cases 1 and 11).

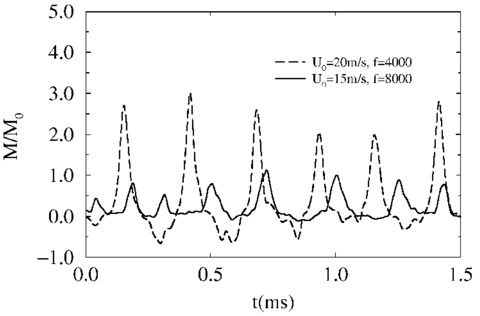

Fig. 8 Effect of forcing amplitude on the momentum flux balance at $x/h = 11.8$ (cases 1 and 12).

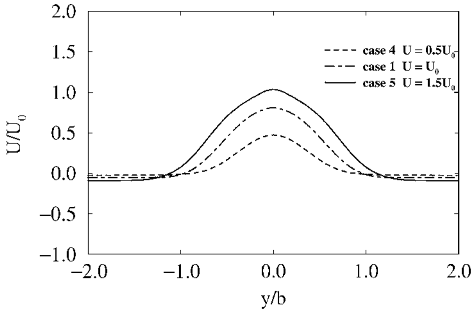

Fig. 9 Mean velocity profile at $x/h = 9.8$ for various forcing amplitudes.

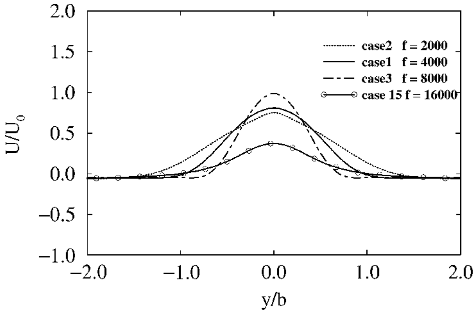

Fig. 10 Mean velocity profile at $x/h = 9.8$ for various forcing frequencies.

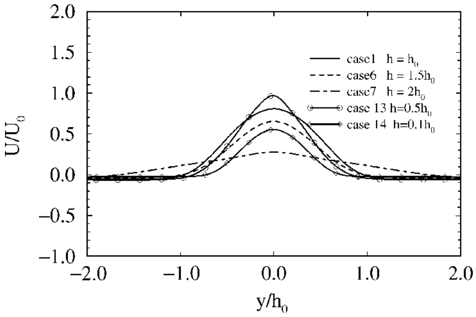

Fig. 11 Mean velocity profile at $x/h = 9.8$ for various orifices.

To determine the efficiency of the actuator and to determine whether general scaling rules can be devised, simulations were also carried out by varying two system parameters such as the forcing amplitude and frequency (cases 12 and 13). Figure 7 shows that increasing forcing amplitude and decreasing the frequency results in a larger momentum flux at a fixed downstream location when the vortex passes by. However, not much change is observed during the in-between period. When the forcing amplitude is decreased and the frequency increased (Fig. 8), the net momentum flux at $x/h = 11.8$ decreases significantly. These results along with the results described earlier suggest that to transfer a large momentum into the flow the amplitude should be increased. (However, the frequency cannot be too high!) Obviously, the exact (optimal) values of these parameters will depend on other variables such as the actuator's natural frequency, material strength of the actuator (to withstand large amplitude oscillation), and the depth of the cavity (because the amplitude of the oscillation of the surface cannot exceed the depth of the cavity).

Time-mean streamwise velocity at the same fixed streamwise location is shown in Figs. 9–11 for some representative cases. It is apparent that the average velocity at any streamwise location, e.g., $x/h = 9.8$, will increase with the forcing amplitude. This is understandable because a larger amount of momentum is transferred with increase in forcing amplitude. However, the spreading of the jet is not significantly affected by the increase in forcing amplitude. When the forcing frequency is changed (Fig. 10), both the peak centerline velocity and the spread of the jet are affected. Jets generated by a high-frequency forcing are narrow with a larger centerline velocity when compared to cases with lower frequencies. This increase in the mean velocity with increase in frequency is related to the fact that the jet gets more energy from a high-frequency forcing over a given time period (for a fixed forcing amplitude). However, as the frequency becomes very high (for example, $f = 16$ kHz) the average velocity decreases. The reason is that the fluid that was driven out from the cavity will be sucked in immediately if the frequency is very high. This implies that there is an upper limit for the forcing frequency. (Of course, structural considerations can impose an even lower limit.)

Figure 11 shows the mean velocity profiles for different orifice size. The peak velocity decreases with increasing orifice size, and this phenomenon is related to the redistribution of the total momentum over a large area. On the other hand, decreasing orifice size initially increases the peak velocity, but as the size becomes very small viscous dissipation begins to dominate, and the peak velocity drops (and is consistent with the earlier momentum analysis).

The phase speed of the vortex ring moving away from the jet orifice for the various cases is computed using two-point correlations. For a reference velocity of $U_0 = 20$ m/s, the phase velocity is around 16.2 m/s for case 1, which is around $0.81U_0$. This is consistent with past observations in forced jet flows. However, the forcing frequency, the amplitude, and the cavity orifice size all impacts the phase speed of the vortex ring. The effect of changing frequency is relatively benign; however, when the forcing amplitude is changed, the phase speed of the vortex ring is changed. This is expected because the motion of the vortex ring is directly proportional to the flow velocity. Making the cavity orifice size larger reduces the phase speed of the vortex ring drastically. This is a result of the redistribution of the momentum in the radial direction making the outward (axial) motion less effective.

These results suggest that in order to maintain a coherent synthetic jet from the orifice all of these parameters need to be optimized carefully. The present study suggests that there is a lower limit for the orifice size and an upper limit for the forcing frequency (keeping all other parameters constant) to get efficient synthetic jet actuation. Increase in the forcing amplitude also provides an efficient momentum transfer mechanism. However, there are likely to be other (nonfluidic) conditions that may restrict the design. For example, the efficiency and capability of the piezoelectric actuator and the structural integrity of the cavity can also be very important for synthetic jet design.

Fuel-Air Mixing Enhancement Using Synthetic Jets

The study just discussed focused on an isolated synthetic jet and evaluated the importance of various system design parameters. Because the eventual goal of this study is to evaluate the impact of synthetic jets fuel–air mixing enhancement, two integrated configurations were simulations. In the first configuration two synthetic jets are placed inside the fuel jet with actuation normal to the primary fuel flow direction, whereas in the second configuration the synthetic jets are placed at the lip of the fuel injector with actuation parallel to the fuel flow direction. Figures 12 and 13 show, respectively, these two configurations schematically. Both configurations are being studied experimently, and results have shown that both result in enhanced mixing. However, the experimental devices are much larger than actual fuel injector size[4] and, therefore, it is not clear whether this observation will hold when the device and the injector are of the actual (i.e., much smaller) scale.

The orifice size is still $h_0 = 0.5$ mm, and the fuel injector size is $3h_0$ with a lip thickness of $2h_0$. Although these values are not fully representative of realistic fuel injector, they do represent a reasonable approximation to a real system. The entire domain shown is simulated (i.e., centerline approximation is not invoked) in order simulate the interaction between the synthetic jet, the primary fuel jet, and the surrounding airstream. A grid of 321 × 425 is used for all of the simulations. With this resolution the cavity region is well resolved by around 20 × 20 grid points, and the synthetic jet orifice is resolved by around 10 grid points.

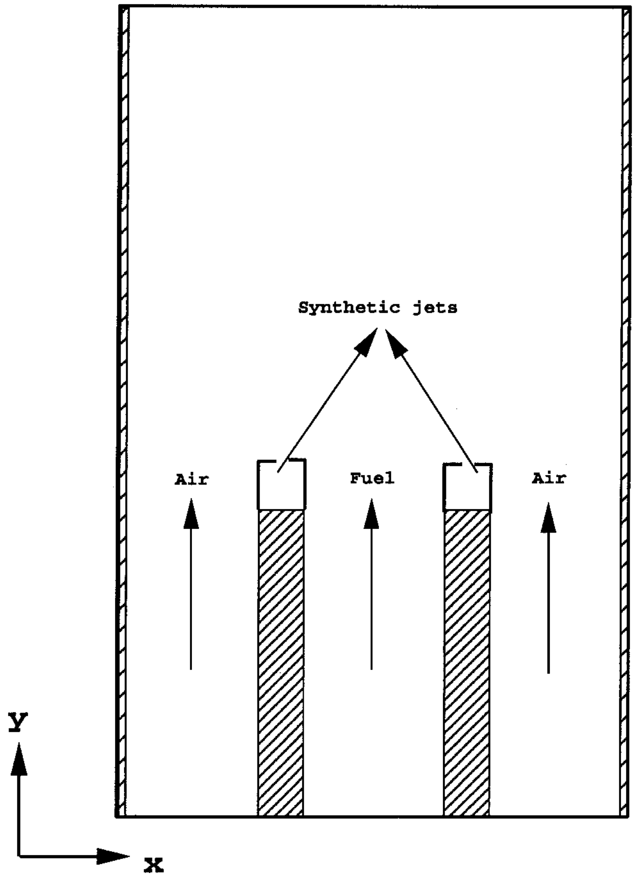

Fig. 13 Computational domain for a fuel injector with two synthetic jets at the lip of the fuel injector (axial case).

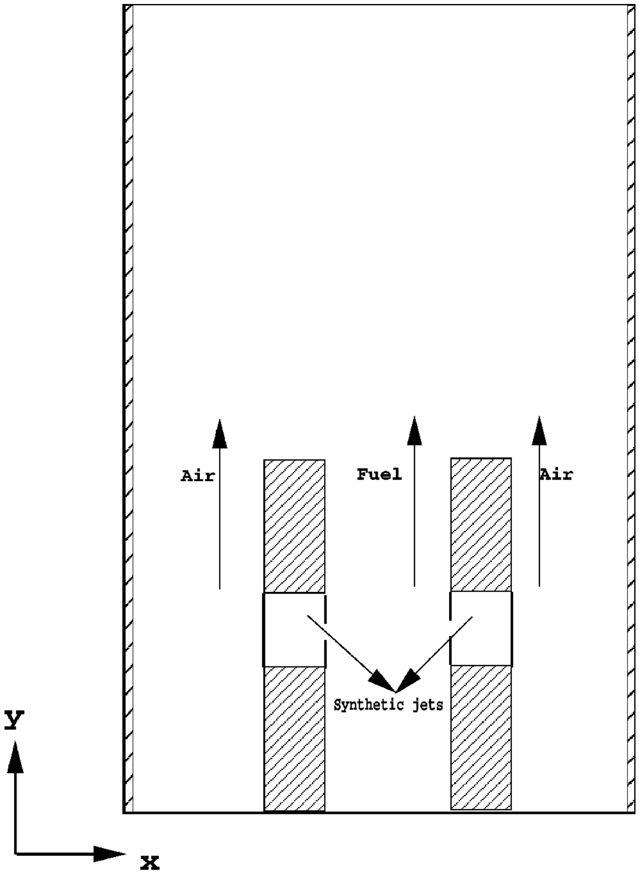

Fig. 12 Computational domain for a fuel injector with two embedded synthetic jets inside the fuel injector (normal case).

When synthetic jets turned on, complex vortex shedding in the near field is observed (not shown). The vortices shed by the synthetic jet trigger an instability in the primary fuel stream. (Note that the primary fuel and surrounding air streams are not forced.) As a result, the primary fuel stream undergoes unstable flapping motion and sheds vortices into the stream. The unforced air jet also undergoes natural instability as a result of the flow around the nozzle lip. Comparison of normally (Fig. 12) and axially (Fig. 13) forced cases shows that normal forcing is much more efficient in triggering complex vortex shedding that enhances the interaction between the fuel stream and the coaxial airstream. The efficiency of the actuation processes is quantified in the next section by analyzing the scalar data in the next section.

Figure 14 compares the fuel mass density for the various normal actuation cases with the unforced case. It can be clearly seen that all of the normal forcing cases show significant spreading of the fuel species. Figure 14 also shows that forcing with just one synthetic jet turned on can result in significant "vectoring" of the fuel stream. This is similar to experimental observations and has important implications for control. Further analysis using scalar fields is described next.

Shear-layer spreading for the axial forcing case is less marked when compared to the normal case, as shown in Fig. 15. Clearly, normal forcing shows significant jet spreading when compared to the axially forced case.

To explain the significant improvement in mixing caused by normal forcing, the flowfield in the vicinity of the injector is analyzed

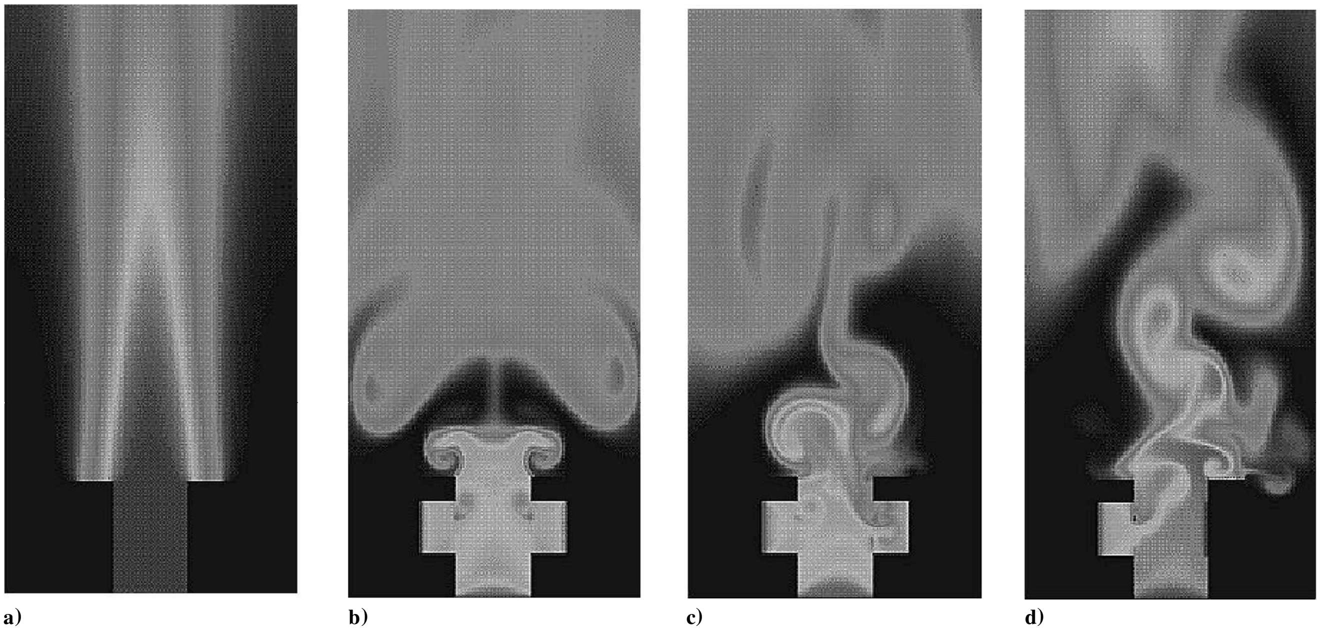

Fig. 14 Comparison of species distribution for four cases: a) unforced case, b) normal forcing in phase, c) normal forcing out of phase, and d) one jetforcing. Here, the central jet in panel a is pure fuel, and the surrounding dark region indicates pure air. Any intermediate gray shade indicates mixed fluid.

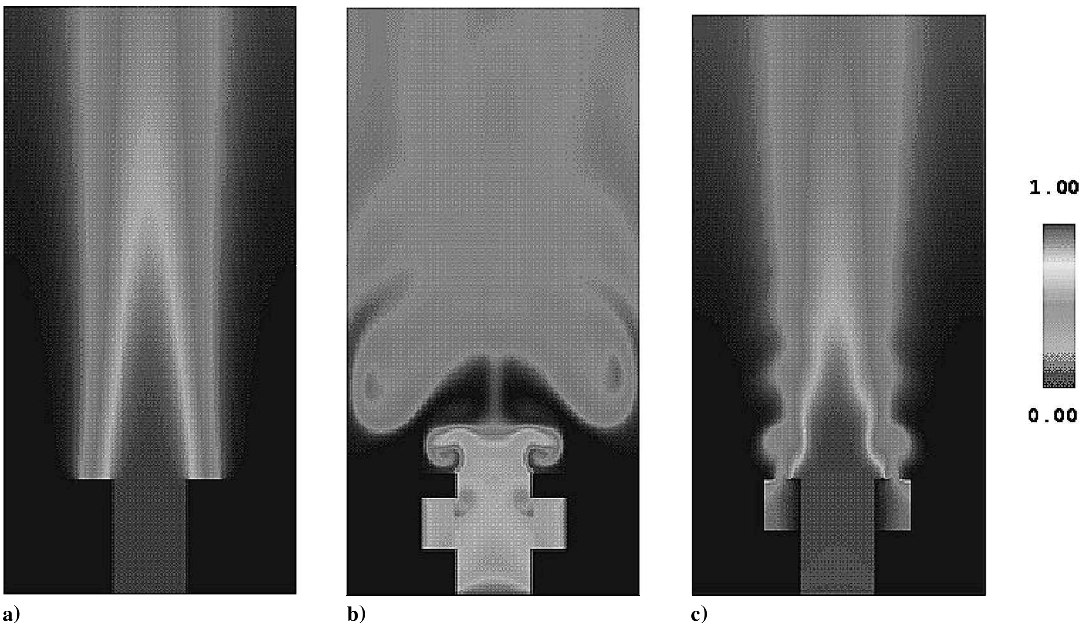

Fig. 15 Comparison of species distribution for the axial and normal forcing case: a) unforced case, b) normal forcing in phase, and c) axial forcing in phase. The gray scale shading is as in the preceding figure.

in detail. Figure 16 shows four instants during a typical forcing cycle. Only the regions of the synthetic jet cavity and the fuel nozzle lip area are shown. The flowfield near the lip clearly shows why the normal forcing case is very effective. During the outward forcing cycle, the fuel stream is pulsed outward, and the fuel spreads outward. However, when the synthetic jet is in its suction mode it causes the air to flow across the fuel lip and into the injector region. This results in a mixed state near and in the exit plane of the fuel nozzle lip, which is then forced outward during the other phase of the forcing cycle. This interaction between the air and fuel is much stronger for the normally forced case than the axially forced case. In the latter case (not shown) forcing is in the direction of the flow, and mixing enhancement occurs in the "conventional" mode, i.e., by entrainment of fuel and air into the shear layer formed downstream of the fuel injector lip. This process is significantly less efficient than the normal forcing case.

The efficiency of the normal injection case can be quantified by evaluating the "mean" scalar field in the region downstream of the fuel injector. The mean field is obtained by averaging the simulation data over 10 cycles. Figures 17 and 18 show, respectively, the fuel density at an axial location for two cases with $u_{\mathrm{fuel}} = u_{\mathrm{air}}$ and $u_{\mathrm{fuel}} = 2u_{\mathrm{air}}$. Clearly, the normal forcing results in significantly enhanced mixing as can be observed by the large increase in spreading of the fuel species density profiles. Although axial forcing also shows increased mixing (when compared to the unforced case), it is apparent that normal forcing is much more efficient in enhancing mixing.

One final comment regarding the normal forced case is that the observed enhancement of mixing is significantly caused by the location of the synthetic jet near the injector lip (the orifice is $2h$ below the lip). If the orifice was located far away (below) the injector lip, then the normal injection may not be very efficient in enhancing mixing

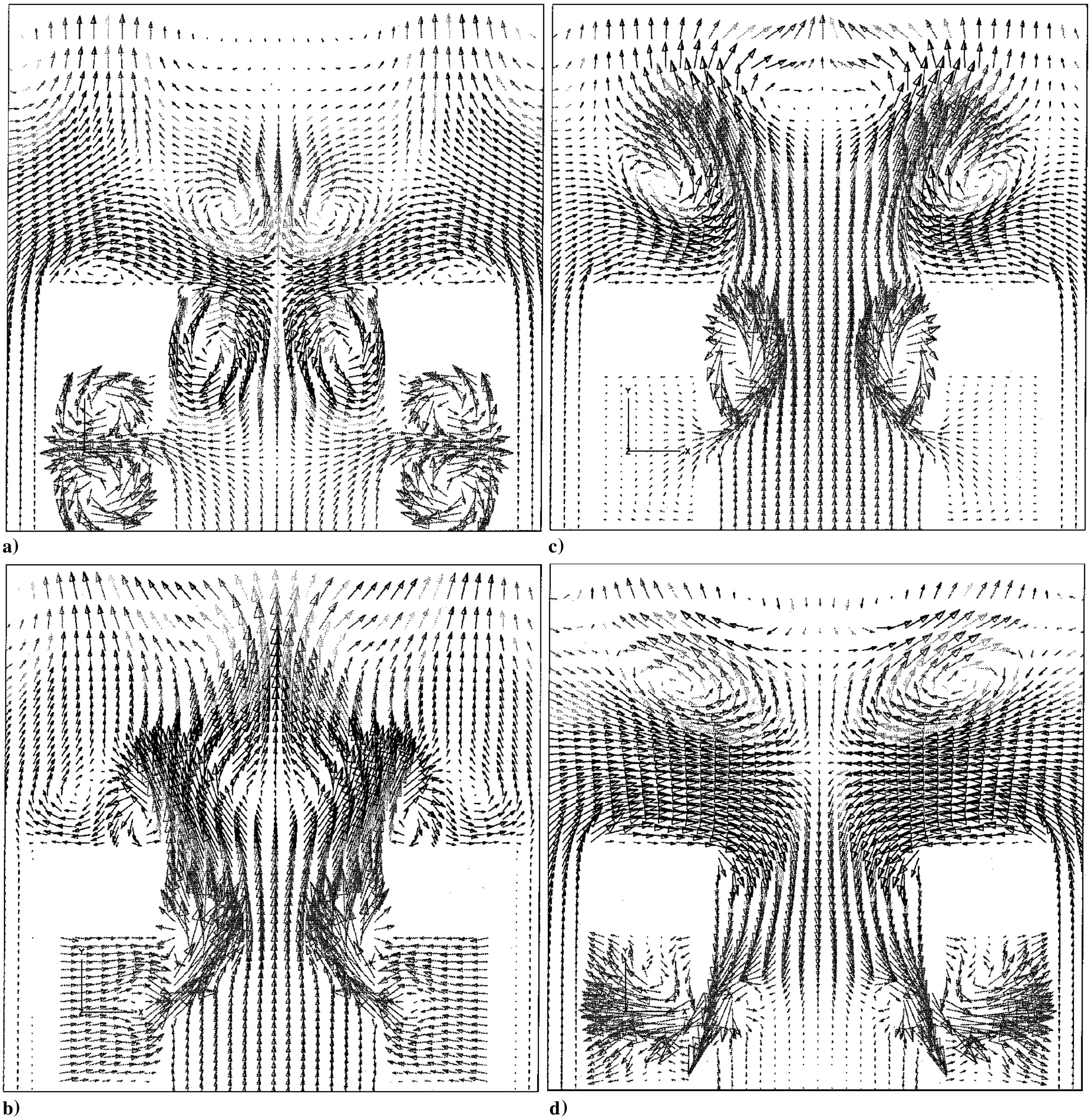

Fig. 16 Velocity vector field (colored by the species mass fraction in the vicinity of the fuel injector for the normal synthetic jet forcing: a) suction mode, b) blowing mode, c) end of the blowing mode, and d) beginning of the suction mode.

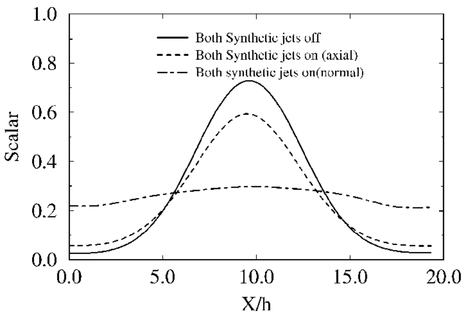

Fig. 17 Species profiles for the axial and normal forcing case (with $u_{\text{fuel}} = u_{\text{air}}$) at $y/d = 13$.

because the synthetic jet will primarily operate on the fuel stream (and will not be able to affect and induce flow of the airstream into the fuel injector region).

Also, the impact of mixing enhancement on combustion remains to be evaluated. However, the present study suggests that if fuel–air mixing can be increased significantly using these MEMS devices then lean combustion can become feasible in gas turbine engines. The implications of achieving stable lean combustion are profound because increase in fuel efficiency will reduce logistic requirements and also result in new lightweight compact engine designs for many practical applications.

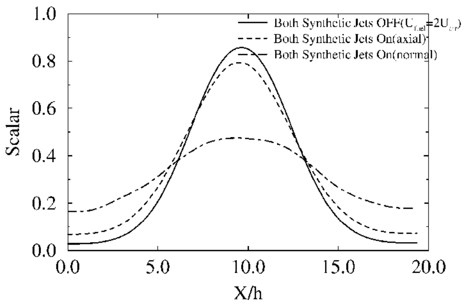

Fig. 18 Species profiles for the axial and normal forcing case (with $u_{\text{fuel}} = 2u_{\text{air}}$) at $y/d = 13$.

Conclusions

In this study a computationally efficient LBE method has been used to simulate microsynthetic jet flows both in isolation and embedded inside fuel injectors. Various design parameters that control system performance are systematically varied in order to determine the efficiency of the synthetic jet actuation. Analysis of the results confirm the ability of the LBE method to capture accurately the dynamics of the synthetic jet induced flowfield at a computational cost that is a fraction of a conventional finite volume approach. The results also have given insight into the sensitivity of the system to design parameters. For example, there is a lower limit on the orifice diameter and an upper limit on the forcing frequency for effective actuation.

The effectiveness of the synthetic jet when implemented inside fuel injector has also been investigated in this study. Both normal and axial forcing of the fuel–air mixing process have been investigated. It is shown that normal forcing within the fuel injector has a marked impact on the mixing process because the periodic pulsing (that includes both outflow and inflow) results in local entrainment of the air and fuel stream that increases the mixing substantially.

Appendix A: Fluid Boundary Conditions for the LBE Models

Proper implementation of boundary conditions is critical for accurate simulations using the Lattice Boltzmann Equation (LBE) method. In addition to the inflow and outflow conditions, the wall conditions have to be implemented correctly. Scalar modeling also requires careful consideration on the application of boundary condition for the mixture and species density. Here we describe in some detail all of these boundary conditions.

The boundary conditions as applied to the synthetic jet case depend also on the orientation of the wall relative to the lattice. As an example, take the case of a node on a wall, as shown in Fig. A1. After streaming, f_0, f_1, f_3, f_4, f_7, f_8 are known but f_2, f_6, and f_5 are not known because they depend on the wall conditions. Suppose that u_x and u_y (the two velocity components) are specified on the wall. (Obviously they will be zero for no slip, but the following derivation allows for slip wall and for wall blowing/suction conditions.) Using Eqs. (4) and (5), we obtain

$$f_2 + f_5 + f_6 = \rho - (f_0 + f_1 + f_3 + f_4 + f_7 + f_8) \quad \text{(A1)}$$

$$f_5 - f_6 = \rho u_x - (f_1 - f_3 - f_7 + f_8) \quad \text{(A2)}$$

$$f_2 + f_5 + f_6 = \rho u_y + (f_4 + f_7 + f_8) \quad \text{(A3)}$$

Further, assuming elastic collision (also called bounce-back assumption, which is reasonable for noncatalytic walls[26]) we get $f_2 - f_2^{(eq)} = f_4 - f_4^{(eq)}$. On combining this relation with Eqs. (A1) and (A3), we obtain

$$\rho = [1/(1 - u_y)][f_0 + f_1 + f_3 + 2(f_4 + f_7 + f_8)] \quad \text{(A4)}$$

$$f_2 = f_4 + \tfrac{2}{3}\rho u_y \quad \text{(A5)}$$

$$f_5 = f_7 - \tfrac{1}{2}(f_1 - f_3) + \tfrac{1}{2}\rho u_x + \tfrac{1}{6}\rho u_y \quad \text{(A6)}$$

$$f_6 = f_8 - \tfrac{1}{2}(f_1 - f_3) - \tfrac{1}{2}\rho u_x + \tfrac{1}{6}\rho u_y \quad \text{(A7)}$$

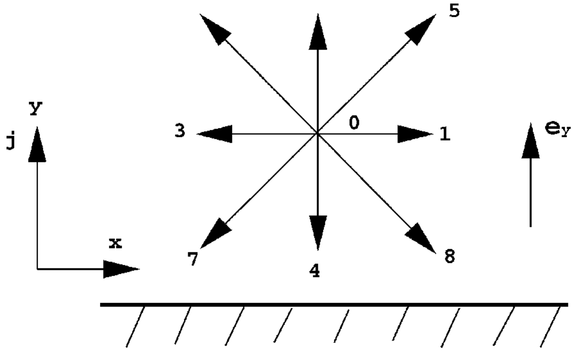

Fig. A1 Schematic of the velocity directions above a no-slip wall.

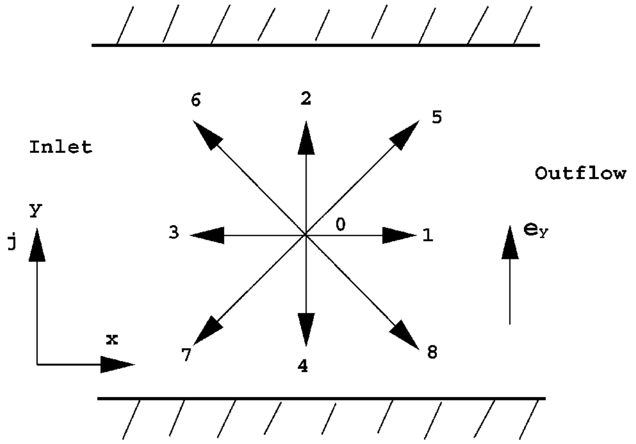

Fig. A2 Schematic plot of velocity directions at inlet and outlet boundary.

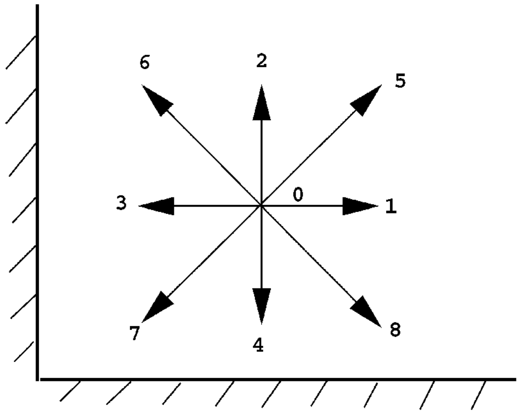

Fig. A3 Schematic plot of the concave corner and velocity directions.

For the inflow and outflow boundary conditions, consider the case shown in Fig. A2. Suppose that u_x and u_y are specified at the inlet, whereas at the outflow they are calculated by a second-order extrapolation of velocity from the interior. Then, after streaming, f_2, f_3, f_4, f_6, f_7, f_0 are known but ρ, f_1, f_5, and f_8 need to be determined. From Eqs. (4) and (5) we get

$$f_1 + f_5 + f_8 = \rho - (f_0 + f_2 + f_3 + f_4 + f_6 + f_7) \quad \text{(A8)}$$

$$f_5 - f_8 = -f_2 + f_4 - f_6 + f_7 \quad \text{(A9)}$$

$$f_1 + f_5 + f_8 = \rho u_x + (f_3 + f_6 + f_7) \quad \text{(A10)}$$

Consistency of Eqs. (A8) and (A10) gives

$$\rho = [1/(1 - u_x)][f_0 + f_2 + f_4 + 2(f_3 + f_6 + f_7)] \quad \text{(A11)}$$

Again, using the bounce-back rule for the nonequilibrium part of the particle distribution normal to the inlet we obtain $f_1 - f_1^{(eq)} = f_3 - f_3^{(eq)}$, and so $f_1 = f_3 + \frac{2}{3}\rho u_x$. Finally, we obtain f_5 and f_8 by substituting f_1 into Eqs. (A8) and (A9):

$$f_5 = f_7 - \tfrac{1}{2}(f_2 - f_4) + \tfrac{1}{6}\rho u_x \quad \text{(A12)}$$

$$f_8 = f_6 + \tfrac{1}{2}(f_2 - f_4) + \tfrac{1}{6}\rho u_x \quad \text{(A13)}$$

The corner nodes (concave and convex corners) also need some special treatment. Consider a concave corner node as an example (Fig. A3). After streaming, f_3, f_4, f_7 are known, ρ is specified, and $u_x = u_y = 0$ for no-slip boundary condition. We need to determine f_1, f_2, f_5, f_6, f_8. Using elastic collision rules for the nonequilibrium part of the particle distribution normal to the inlet and to the boundary, we obtain $f_1 = f_3 + (f_1^{eq} - f_3^{eq}) = f_3$ and $f_2 = f_4 + (f_2^{eq} - f_4^{eq}) = f_4$. Using f_1, f_2 from the preceding relation, we obtain

$$f_5 = f_7$$

$$f_6 = f_8 = \tfrac{1}{2}[\rho_{\text{in}} - (f_0 + f_1 + f_2 + f_3 + f_4 + f_5 + f_7)] \quad \text{(A14)}$$

Appendix B: Scalar Boundary Conditions for LBE models

To apply scalar boundary conditions at a noncatalytic wall (given by zero wall normal scalar gradient), a method similar to earlier ones[26,29,30] is employed. Consider the wall as shown in Fig. A1. After streaming, f_0, f_1, f_3, f_4, f_7, f_8 are known, but f_2, f_6, and f_5 are not because they depend upon the wall conditions. In the following the distribution function f_i is actually $f_i{}^2$, and all variables ($\rho = \rho^2$) are for scalar field.

The elements of the distribution function can be classified into three groups, f_+^j, f_-^j, and f_0^j, according to the sign of $\boldsymbol{e}_\alpha \cdot \boldsymbol{e}_y$. For the case in Fig. A1, f_+^j, includes f_2^j, f_5^j, and f_6^j and f_-^j includes f_4^j, f_7^j, and f_8^j, whereas f_0^j includes f_0^j, f_1^j, and f_3^j. The spatial dependence on y direction is noted by superscript j. Equation (8) can be changed into the following form:

$$f_\pm^{j+1} - f_\pm^j = (1/\tau)\left[f_\pm^j - f_\pm^{j(eq)}\right], \qquad f_0^j = f_0^{j(eq)} \tag{B1}$$

The passive scalar boundary condition is specified by setting the passive scalar at the wall equal to the grid point immediately above the wall, that is, $\rho^j = \rho^{j+1}$. Here, ρ^j is the scalar density at the jth position.

The density profile of the passive scalar can be obtained from Eq. (B1). We sum all of the elements of the distribution in each of the groups and define the sum as $F_\pm^j = \Sigma f_\pm^j$. For the case shown in Fig. A2, we have $F_+^{j(eq)} = f_2^{j(eq)} + f_5^{j(eq)} + f_6^{j(eq)}$ and $F_-^{j(eq)} = f_4^{j(eq)} + f_7^{j(eq)} + f_8^{j(eq)}$. Applying no-slip wall condition into Eq. (3), we can find that

$$f_2^{j(eq)} = f_4^{j(eq)} = \rho^j/9 \tag{B2}$$

$$f_5^{j(eq)} = f_6^{j(eq)} = f_7^{j(eq)} = f_8^{j(eq)} = \rho^j/36 \tag{B3}$$

Combining Eqs. (B2) and (B3) with the preceding relations, we get $F_\pm^{j(eq)} = \rho^j/6$. From Eq. (3) and the second part of Eq. (B1) (with no-slip wall condition), we have

$$f_0^j = f_0^{eq} = \tfrac{4}{9}\rho^j \tag{B4}$$

$$f_1^j = f_1^{j(eq)} = \tfrac{1}{9}\rho^j \tag{B5}$$

$$f_3^j = f_3^{j(eq)} = \tfrac{1}{9}\rho^j \tag{B6}$$

Summing Eqs. (B4–B6), we obtain $F_0^j = f_0^j + f_1^j + f_3^j = \frac{2}{3}\rho^j$; substituting $F_\pm^j = \Sigma f_\pm^j$ into Eq. (4) gives $F_+^j + F_-^j + F_0^j = \rho^j$; and combining these two relations results in $F_+^j + F_-^j = \rho^j/3$. Therefore, at the boundary ($j = 0$) the following condition must be satisfied for scalar: $F_+^0 + F_-^0 = \rho^0/3$. In the simulation the scalar boundary condition is implemented by computing the unknown distribution function elements in the group f_+^j by the following equation:

$$f_a^0 = 2w_a\rho^0 - f_b^0 \tag{B7}$$

and then updating it using Eq. (2). Here, w_a are the weights, and a and b are any pair of indices such that e_a and e_b are mirror images of each other with respect to the wall. For the case shown in Fig. A1, the mirror images of f_2^0, f_5^0, and f_6^0 are f_4^0, f_8^0, and f_7^0, respectively. For the case shown in Fig. A1, we have

$$f_2^0 = \tfrac{2}{9}\rho^0 - f_4^0, \qquad f_5^0 = \tfrac{2}{36}\rho^0 - f_8^0, \qquad f_6^0 = \tfrac{2}{36}\rho^0 - f_7^0 \tag{B8}$$

where ρ^0 is known from the wall boundary condition as $\rho^0 = \rho^1$. Summing the equations in Eq. (B8), we obtain

$$f_2^0 + f_5^0 + f_6^0 + f_4^0 + f_8^0 + f_7^0 = \tfrac{1}{3}\rho^0 \tag{B9}$$

Because $F_+^0 = f_2^0 + f_5^0 + f_6^0$ and $F_-^0 = f_4^0 + f_8^0 + f_7^0$, Eq. (B9) can be simplified to the following equation:

$$F_+^0 + F_-^0 = \tfrac{1}{3}\rho^0 \tag{B10}$$

which satisfies the scalar boundary condition at the wall as defined earlier.

Acknowledgments

This work was supported by the Army Research Office under Grant DAAG55-98-1-0495 and monitored by David Mann.

References

[1] Ho, C.-M., and Tai, Y.-C., "Review: MEMS and Its Applications for Flow Control," *Journal of Fluids Engineering*, Vol. 118, No. 3, 1996, pp. 437–447.

[2] Tseng, F.-G., Linder, C., Kim, C.-J., and Ho, C.-M., "Control of Mixing with Micro Injectors for Combustion Applications," *Dynamic Systems and Control*, Vol. 59, 1996, pp. 183–187.

[3] Smith, B. L., and Glezer, A., "Vectoring and Small-Scale Motions Effected in Free Shear Flows Using Synthetic Jet Actuators," AIAA Paper 97-0213, Jan. 1997.

[4] Smith, B. L., and Glezer, A., "The Formation and Evolution of Synthetic Jets," *Physics of Fluids*, Vol. 10, No. 9, 1998, pp. 2281–2297.

[5] Kral, L., Donovan, J. F., Coin, A. B., and Cary, A. W., "Numerical Investigation of Synthetic Jet Flowfields," AIAA Paper 97-1824, June 1997.

[6] Rizzetta, D. P., Visbal, M. R., and Stanek, M. J., "Numerical Investigation of Synthetic Jet Flowfields," *AIAA Journal*, Vol. 37, No. 8, 1999, pp. 919–927.

[7] Lee, C. Y., and Goldstein, D. B., "Two-Dimensional Synthetic Jet Simulations," AIAA Paper 2000-0406, Jan. 2000.

[8] Chen, H., Chen, S., and Matthaeus, W. H., "Recovery of the Navier–Stokes Equations Using a Lattice Boltzmann Method," *Physical Review A : General Physics*, Vol. 45, No. 4, 1991, pp. R5339–R5342.

[9] Chen, S., Wang, J., Doolen, G., and Shan, X., "Lattice Boltzmann Computational Fluid Dynamics in Three Dimensions," *Journal Statistical Physics*, Vol. 68, No. 3/4, 1992, pp. 379–400.

[10] Shan, X., and Chen, H., "Lattice Boltzmann Model for Simulating Flows with Multiple Phases and Components," *Physical Review E*: Vol. 47, No. 3, 1993, pp. 1815–1819.

[11] Chen, S., Dawson, S. P., Doolen, G., Janecky, D. R., and Lawniczak, A., "Lattice Methods and Their Applications to Reacting Systems," *Computers in Chemical Engineering*, Vol. 19, No. 6–7, 1995, pp. 617–646.

[12] Chen, S., and Doolen, G., "Lattice Methods and Their Applications to Reacting Systems," *Annual Review of Fluid Mechanics*, Vol. 30, 1998, pp. 329–364.

[13] Menon, S., and Calhoon, W., "Subgrid Mixing and Molecular Transport Modeling for Large-Eddy Simulations of Turbulent Reacting Flows," *Proceedings of the Combustion Institute*, Vol. 26, 1996, pp. 59–66.

[14] Chakravarthy, V., and Menon, S., "Subgrid Modeling of Turbulent Premixed Flames in the Flamelet Regime," *Flow, Turbulence and Combustion*, Vol. 65, No. 2, 2000, pp. 133–161.

[15] Noble, N. R., Chen, S., Georgiadis, J. G., and Buckuis, R., "A Consistent Hydrodynamic Boundary Condition for the Lattice Boltzmann Method," *Physics of Fluids*, Vol. 7, No. 1, 1995, pp. 203–209.

[16] Zou, Q., Hou, S., Chen, S., and Doolen, G. D., "An Improved Incompressible Lattice Boltzmann Model for Time Dependent Flows," *Journal of Statistical Physics*, Vol. 81, No. 1/2, 1995, pp. 35–48.

[17] Alexander, F., Chen, H., Chen, S., and Doolen, G., "A Lattice Boltzmann Model for Compressible Fluid Flows," *Physical Review A: General Physics*, Vol. 46, No. 4, 1992, pp. 1967–1978.

[18] He, X., and Luo, L.-S., "Theory of the Lattice Boltzmann Method: from the Boltzmann Equation to the Lattice Boltzmann Equation," *Physical Review E*, Vol. 56, No. 6, 1997, pp. 6811–6817.

[19] Qian, Y. H., d'Humières, D., and Lallemand, P., "Lattice BGK Models for the Navier–Stokes Equation," *Europhysics Letters*, Vol. 17, No. 4, 1992, pp. 479–484.

[20] He, X., and Luo, L.-S., "A Priori Derivation of the Lattice Boltzmann Equation," *Physical Review E*, Vol. 55, No. 6, 1997, pp. R6333–R6336.

[21] Qian, Y. H., and Zhou, Y., "Complete Galilean-Invariant Lattice BGK Models for Navier–Stokes Equations," *Europhysics Letters*, Vol. 42, No. 4, 1998, pp. 359–364.

[22] Filippova, O., and Hanel, D., "A Novel Lattice BGK Approach for Low Mach Number Combustion," *Journal of Computational Physics*, Vol. 158, No. 2, 2000, pp. 139–160.

[23] He, X., "Error Analysis for the Interpolation-Supplemented Lattice Boltzmann Equation Scheme," *International Journal of Modern Physics C*, Vol. 8, No. 4, 1997, pp. 737–745.

[24] Ginzbourg, I., and d'Humieres, D., "Local Second-Order Boundary Methods for Lattice Boltzmann Models," *Journal of Statistical Physics*, Vol. 84, No. 5/6, 1996, pp. 927–971.

[25] Zou, Q., and He, X., "On Pressure and Velocity Boundary Conditions for the Lattice Boltzmann BGK Model," *Physics of Fluids*, Vol. 9, No. 6, 1997, pp. 1591–1598.

[26] Shan, X., "Simulation of Rayleigh-Benard Convection Using a Lattice Boltzmann Method," *Physical Review E*, Vol. 55, No. 3, 1997, pp. 2780–2788.

[27] He, X., Luo, L., and Dembo, M., "Some Progress in Lattice Boltzmann Method: Part I. NonUniform Mesh Grids," *Journal of Computational Physics*, Vol. 129, No. 2, 1996, pp. 357–363.

[28] He, X., and Doolen, G. D., "Lattice Boltzmann Method on Curvilinear Coordinates System: Flow Around a Circular Cylinder," *Journal of Computational Physics*, Vol. 134, No. 2, 1997, pp. 306–315.

[29] He, X., Chen, S., and Doolen, G. D., "A Novel Thermal Model for the Lattice Boltzmann Method in Incompressible Limit," *Journal of Computational Physics*, Vol. 146, No. 1, 1998, pp. 282–300.

[30] He, X., and Li, N., "Lattice Boltzmann Simulation of Electrochemical Systems," *Computer Physics Communications*, Vol. 129, No. 1–3, 2000, pp. 158–166.

[31] Gutmark, E., and Ho, C.-M., "Preferred Modes and the Spreading Rates of Jets," *Physics of Fluids*, Vol. 26, No. 10, 1983, pp. 2932–2938.

[32] Menon, S., "Fuel–Air Mixing Enhancement Using Synthetic Microjets," Computational Combustion Lab., CCL-00-002, Dept. of Aerospace Engineering, Georgia Inst. of Technology, Atlanta, GA, 2000.

S. K. Aggarwal
Associate Editor